IEEE Access
Multidisciplinary | Rapid Review | Open Access Journal

Received January 2, 2021, accepted January 12, 2021, date of publication January 18, 2021, date of current version January 26, 2021.

*Digital Object Identifier 10.1109/ACCESS.2021.3052545*

# Comparative Analysis of Different Permanent Magnet Arrangements in a Novel Flux Modulated Electric Machine

**JIAHUI HUANG, WEINONG FU, SHUANGXIA NIU, (Senior Member, IEEE), AND XING ZHAO, (Member, IEEE)**

Department of Electrical Engineering, The Hong Kong Polytechnic University, Hong Kong

Corresponding author: Weinong Fu (eewnfu@polyu.edu.hk)

This work was supported by the Research Grant Council of the Hong Kong Special Administrative Region (SAR) Government under the project PolyU 152185/18E.

**ABSTRACT** A novel dual permanent magnet (PM) machine with Halbach segmentation flux modulation is proposed in this paper, which is evolved from a flux switching PM machine (FSPM). In order to improve the performance of the FSPM, several PM arrangement methods have been adopted and three new different structures have been investigated. To achieve a fair comparison, all the structures are under the same size and rotate at the same speed. The performances of output torque and back EMF are compared. The analysis results show that the dual PM with Halbach segmentation has the highest torque density and power efficiency. The torque is improved by 100.3% from the FSPM while the PM volume does not increase too much. The unique of this best structure is that it not only combines the vernier machine and FSPM machine together, but also reduces the torque ripple. The performance of the motor is verified by the simulation using finite-element analysis (FEA).

**INDEX TERMS** Dual PM, electric machines, finite element methods, permanent magnet machines, torque density.

## I. INTRODUCTION

With the emergence and development of renewable energy and automation technology, electric machines have attracted more and more attention. They play important roles in many applications, such as electric vehicles, drones, wind power generators, industrial robots, etc [1]–[4]. To meet the requirements for high torque density and efficiency in these applications, the conventional PM machines have been widely used. However, to further increase the torque density in the conventional structures without sacrificing the power efficiency has already been constricted. There are two main restrictions in conventional PM machines. One is the pole-pair number of the stator should equal the rotor pole pair number, which leads to the increased copper loss when increasing the rotor poles number. The other is the limited space to employ more PMs.

Flux-modulated PM machines are a promising solution and have been widely studied. Several different kinds of flux-modulated machines have emerged, including magnetic-geared motor [5], basic flux-modulated motor [6], vernier motor [7]–[10], flux-switching motor [11]–[13], and doubly fed magnetic reluctance machine [14]–[16]. All of these machines are based on the working principle of the novel magnetic gear proposed in [17] and the derivation from it. These machines break the conventional pole-pair combination limitation and a unified theory of them has been proposed [18].

To further optimize the torque density, flux-modulated dual-PM-excited structures have been investigated. The machines have PMs mounted both in rotor and in stator. A basic dual-PM-excited motor is presented in [19], the PMs on the stator are modulated by the rotor teeth, so that the rotor should have salient poles to produce the varying magnetic reluctance. And the stator teeth modulate the magnetic field produced by the rotor PMs at the same time. In [20], a design method of the vernier machine with dual PM was proposed. And [21] also revealed that the dual PM vernier machine has a better performance than stator-PM and rotor-PM machines. In [22], several dual-PM-excited motors have different stator structures with the same rotor are comparatively studied. The comparison results show the motor with stator PMs located on the tooth region has the best performance.

The researches on the PM arrangements in different machines have never stopped. In [23], different PM arrangements in the stator back iron have been investigated and compared. The results show that the V-shaped PM arrangement

The associate editor coordinating the review of this manuscript and approving it for publication was Paolo Giangrande.

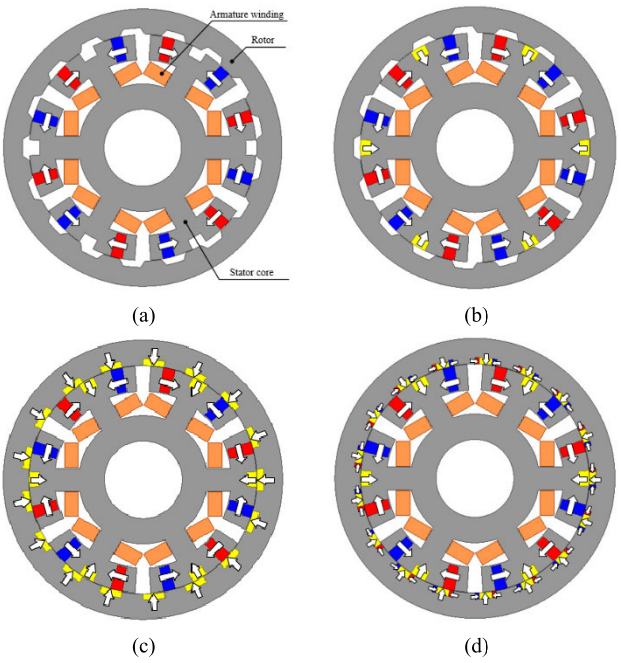


**FIGURE 1.** Structures of the proposed flux modulated machines. (a) Outer rotor FSPM. (b) Outer rotor FSPM with middle stator PM. (c) Dual PM flux modulated machine. (d) Dual PM flux modulated machine with Halbach segmentation.

has the best performance compared to the arc-shaped and I-shaped. The PM arrangements in rotor has also been investigated in [24]. To reduce the torque ripple and asymmetric phase back-EMF caused by the consequent pole, different PM arrangements in rotors have been investigated and a hybrid pole structure has been proposed.

This paper proposes several PM arrangement methods to improve machine performance. New structures of the flux-modulated machine are proposed, and the best structure is featured by dual PM with Halbach segmentation. It not only improves the torque density but also reduces the harmonics. The paper is organized as follows. Firstly, the topologies of machines will be introduced. Next, the operating principle will be illustrated. Then, the performance of all topologies will be compared. Moreover, the detailed analysis of design parameters for the best structure will be conducted. Finally, the conclusion will be drawn.

## II. MACHINE TOPOLOGIES

A multi-tooth FSPM was proposed in [25] which is derived from 6 slots 17 rotor teeth V-shaped FSPM. To increase the torque density, a new outer rotor FSPM (Machine 1) is proposed based on the existing FSPM. As shown in Fig. 1(a), the air gap radius is increased a lot when adopting outer rotor structure. This structure also eliminates the influence caused by relatively complex and space-consuming stator structure of the inner rotor FSPM. To further increase the output torque, a middle magnet is added in each stator dummy slot (Machine 2). The structure is shown in Fig.1(b).

It is well known that the average torque $T_{ave}$ can be obtained by the equation

$$T_{ave} = \frac{m}{\sqrt{2}} L_s D N_{ph} I_{rms} B_g K_w \tag{1}$$

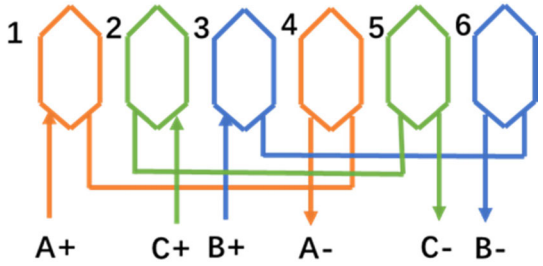


**FIGURE 2.** Machine winding configuration.

where $m$ is the phase number, $L_s$ is the stack length, $D$ is the air gap diameter, $N_{ph}$ is the turns per phase, $B_g$ is the air gap flux density, and $K_w$ is winding factor. If we keep the same current, we can improve the torque by enhancing the magnetic flux density in the air gap. Employing more PMs is an effective method to improve the toque without consuming the operating energy. Therefore, the dual PM modulated machine (Machine 3) is proposed and shown in Fig. 1(c). To further enhance the output torque, the Halbach magnetization array is adopted in the rotor PM (Machine 4). It reduces the harmonic and increases the flux density in the air gap. The structure is shown in Fig. 1(d).

### A. WINDING CONFIGURATION

According to the working principle of general flux-modulated machines [18], the modulated harmonics will couple together and produce the effective torque. The general relationship between each part is as

$$P_{Fe} = P_1 \pm P_2 \tag{2}$$

Applied to this structure it can be expressed as

$$P_r = P_s \pm P_a \tag{3}$$

where $P_r$ is the number of rotor pole pairs, $P_s$ is the number of stator PMs pole pairs and $P_a$ is the number of armature pole pairs. The winding configuration is shown in Fig. 2. The winding factor is 0.933. This winding topology is employed for all considered machine topologies.

### B. MAIN DESIGN PARAMETERS

To make a relatively fair comparison, the proposed structures are in the same size and rotate at the same speed, in which the outer diameter is 220mm, the stack length is 45mm, and the rotation speed is 800rpm. The inner diameter of the rotor and electric load also keep constant. The main design parameters of the machines are given in Table 1.

## III. OPERATING PRINCIPLE

The operating principle of the proposed machines is based on the general modulated theory. To clearly explain the working principle of the proposed machine, the no-load flux path is presented in Fig. 3. And Fig.4. shows the partial enlarged flux when the rotor is at the aligned position and unaligned position.

To illustrate the operating principle more clearly, the analytical method and 2-D EFA method are applied. The PMs are divided into three groups, namely, $PM_{s1}$, $PM_{s2}$ and $PM_r$.

**TABLE 1. Main design parameters.**

| Parameter | Unit | Value |
|---|---|---|
| Rotor teeth number | / | 17 |
| Stator slots number | / | 6 |
| Machine outer diameter | mm | 220 |
| Machine inner diameter | mm | 61.1 |
| Stack length | mm | 45 |
| Air gap length | mm | 0.45 |
| Slot filling factor | / | 0.5 |
| Rated speed | rpm | 800 |
| Electric load | A | 10990 |
| Current density | A/mm$^2$ | 3.42 |
| PM material | / | N38EH |
| Core material | / | WG35WW300 |

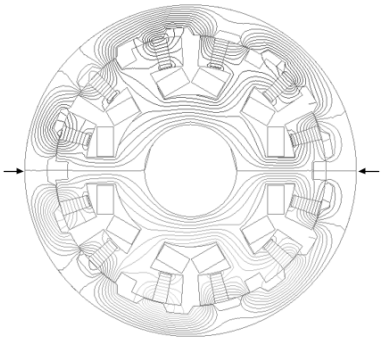

**FIGURE 3. No-load flux path.**

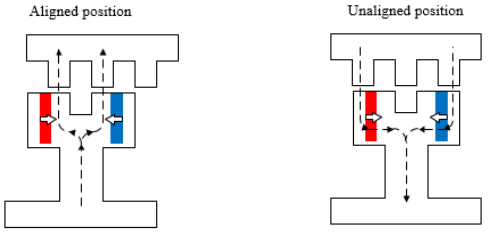


**FIGURE 4. Partial enlarged no-load flux path.**

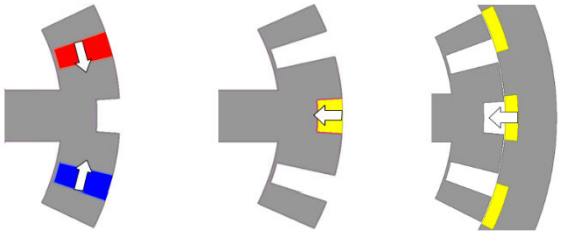


**FIGURE 5. Magnet groups. (a) PM$_{s1}$. (b) PM$_{s2}$ (c) PM$_r$.**

As shown in Fig. 5, PM$_{s1}$ is the pair of flux focusing PMs, PM$_{s2}$ refers to the PM in the stator dummy slot, and PM$_r$ represents the rotor PMs.

The air gap flux density can be obtained by multiplying the magnetomotive force (MMF) and corresponding permeance. When we remove other PMs, the magnetic field excited by PM$_{s1}$ is modulated by rotor teeth. The MMF of PM$_{s1}$ is assumed as a square waveform which is shown in Fig. 6.

In Fig. 6 $N_{slot}$ is the number of slots, $\theta_1$ and $\theta_2$ are the mechanical angles presented in Fig. 7. $F_{s1}$ and $F_{s2}$ refer to the MMF values in different positions.

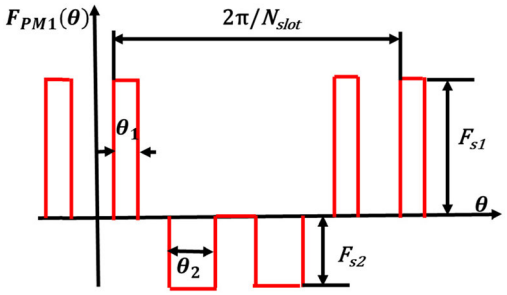


**FIGURE 6. MMF of PM$_{s1}$.**

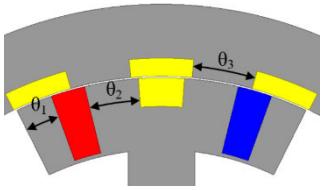


**FIGURE 7. Partial enlarged of stator and rotor.**

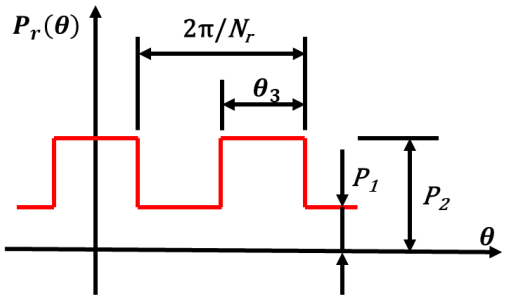


**FIGURE 8. Rotor permeance.**

The MMF of PM$_1$ can be expressed as

$$F_{PM1(\theta)} = \sum_{n=1}^{+\infty} F_n \cos\left(nN_{slot}\theta\right) \tag{4}$$

The permeance of the rotor is given in (5) and the waveform is shown in Fig. 8, where $N_r$ is the number of rotor teeth, $P_1$ is the permeance between rotor teeth and $P_2$ is the permeance in rotor teeth.

$$P_{r(\theta)} = \frac{P_1 + P_2}{2} + \sum_{k=1}^{+\infty} A_k \cos\left(kN_r\theta\right) \tag{5}$$

The air gap field from PM$_{s1}$ can be obtained by:

$$\begin{aligned} B_{PM1(\theta)} &= F_{PM1(\theta)} P_{r(\theta)} \\ &= \frac{P_1 + P_2}{2} \sum_{n=1}^{+\infty} F_n \cos\left(nN_{slot}\theta\right) \\ &\quad + \sum_{\substack{n=-\infty \\ n\neq 0}}^{+\infty} \sum_{k=1}^{+\infty} \frac{F_n A_k}{2} \cos\left(kN_r + nN_{slot}\right)\theta \end{aligned} \tag{6}$$

Similarly, the MMF of PM$_{s2}$ is expressed in Fig. 9 and (7).

$$F_{PM2(\theta)} = \sum_{n=1}^{+\infty} G_n \cos\left(nN_{slot}\theta\right) \tag{7}$$

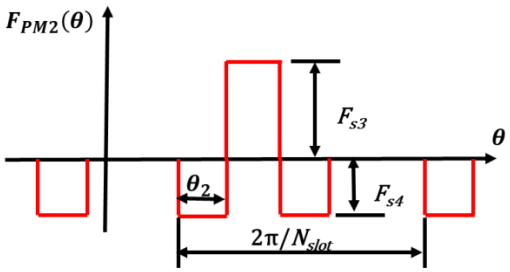


**FIGURE 9.** MMF of $PM_{s2}$.

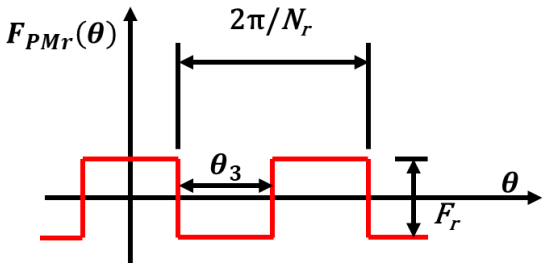


**FIGURE 10.** MMF of $PM_r$.

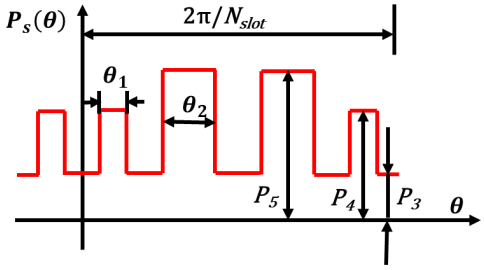


**FIGURE 11.** Permeance of stator.

Compared (4) and (7), the harmonic order of magnetic field produced by $PM_{s2}$ is the same as the $PM_{s1}$.

The MMFs of $PM_r$ and stator permeance are presented in Fig. 10 and 11. $F_r$ is the MMF value of rotor PM. $P_3$, $P_4$ and $P_5$ represent the permeance in different positions of stator teeth.

According to Fig. 10 and Fig. 11, the MMF of $PM_r$ and stator core permeance can be expressed as below

$$F_{PMr(\theta)} = \sum_{n=1}^{+\infty} H_n \cos(nN_r\theta) \tag{8}$$

$$P_{s(\theta)} = P_0 + \sum_{k=1}^{+\infty} C_k \cos(kN_{slot}\theta) \tag{9}$$

where $P_0$ means the average value of permeance in the waveform.

Hence, the air gap flux density produced by $PM_r$ can be obtained

$$\begin{aligned} B_{PMr(\theta)} &= F_{PMr(\theta)} P_{s(\theta)} \\ &= P_0 \sum_{n=1}^{+\infty} F_n \cos(nN_r\theta) \\ &\quad + \sum_{\substack{n=-\infty \\ n\neq 0}}^{+\infty} \sum_{k=1}^{+\infty} \frac{H_n C_k}{2} \cos(kN_{slot} + nN_r)\,\theta \end{aligned} \tag{10}$$

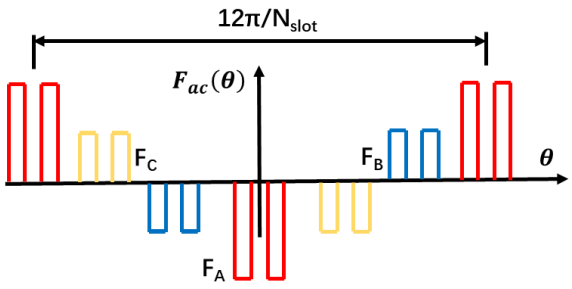


**FIGURE 12.** MMF of armature current.

**TABLE 2.** Harmonic order from different sources.

| Excitation sources | Harmonic order |
|---|---|
| $PM_{s1}$ | $kN_r \pm nN_{slot}$ |
| $PM_{s2}$ | $kN_r \pm nN_{slot}$ |
| $PM_r$ | $kN_{slot} \pm nN_r$ |
| Armature winding | $kN_r \pm \frac{n}{6}N_{slot}$ |

The MMF of armature current in each phase can be expressed as

$$F_A = I_{ac}N_t \cos(2\pi ft) \tag{11}$$

$$F_B = I_{ac}N_t \cos\left(2\pi ft - \frac{2\pi}{3}\right) \tag{12}$$

$$F_c = I_{ac}N_t \cos\left(2\pi ft + \frac{2\pi}{3}\right) \tag{13}$$

where $N_t$ is the number of turns in the coil.

According to [26], [27], to simplify the analysis, let t = 0. The corresponding MMF is shown in Fig. 12.

The simplified MMF of armature current is

$$F_{ac(\theta)} = \sum_{n=1}^{+\infty} I_n \cos\left(\frac{n}{6}N_{slot}\theta\right) \tag{14}$$

The flux density can be obtained as

$$\begin{aligned} B_{ac(\theta)} &= F_{ac(\theta)} P_{r(\theta)} \\ &= \frac{P_1 + P_2}{2} \sum_{n=1}^{+\infty} I_n \cos\left(\frac{n}{6}N_{slot}\theta\right) \\ &\quad + \sum_{\substack{n=-\infty \\ n\neq 0}}^{+\infty} \sum_{k=1}^{+\infty} \frac{I_n A_k}{2} \cos\left(kN_r + \frac{n}{6}N_{slot}\right)\theta \end{aligned} \tag{15}$$

To sum up, the harmonic order of air gap flux density from different sources can be summarized and listed in Table 2.

Fig. 13. presents the air gap flux density and corresponding harmonic order of different excitation sources. They are conducted by using the FEA software. The results of FEA software perfectly match the analyzed results in Table 2.

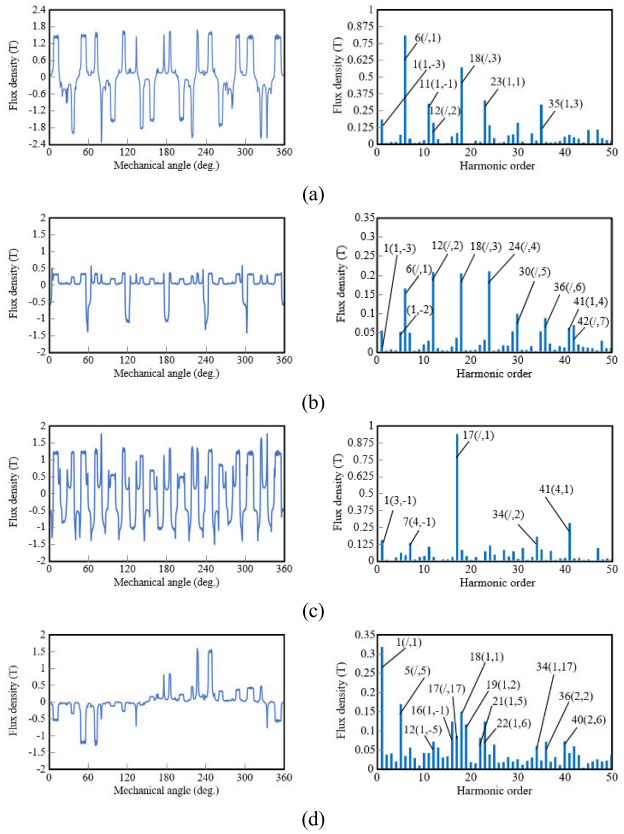


**FIGURE 13.** Flux density in air gap and its corresponding Fast Fourier Transform (FFT) results by different excitation sources. (a) Excited by $PM_{s1}$. (b) Excited by $PM_{s2}$. (c) Excited by $PM_r$. (d) Excited by AC.

## IV. PERFORMANCE ANALYSIS

In this part, the electromagnetic performances of the proposed structures are analyzed. With the commercial software ANSYS Maxwell, the 2-D time-stepping FE analysis is conducted. All the proposed structures rotate at same rated speed and are excited under the same electric load as shown in Table 1.

Fig. 14 compares the torque performance among all structures under the same electric load. It is clear that Machine 4 has the highest output torque, which increases 89.91% from Machine 1. The torques of Machine 2 and Machine 3 are also increased 37.6% and 67% while compared to Machine 1. As analyzed in III, the PMs can be divided into three groups. Machine 3 and Machine 4 adopt all the three groups of PMs and coupled with the armature winding to produce the output torque. Therefore, they have higher output torque than Machine 1 and Machine 2 since Machine 1 only uses one group of magnets and Machine 2 adopts 2 groups. In addition, Machine 4 adopts a Halbach arrangement in the rotor PMs, the air gap flux density has been strengthen. So, Machine 4 has the highest output torque.

It also can be observed that, Machine 3 has the lowest torque ripple while Machine 4 has the highest one.

Fig.15 shows the waveform of cogging torque. It is obviously that Machine 4 has the largest cogging torque, which is 19.17Nm (peak to peak). And Machine 1 has the lowest cogging. From above, Machine 4 has the highest torque and largest cogging while Machine 1 has the lowest torque and cogging at the same time. Machine 3 has the relatively high torque and lowest ripple. The detailed comparison is listed in Table 3.

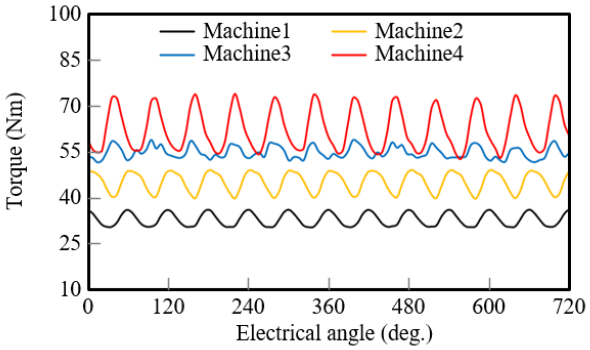


**FIGURE 14.** Torque performance.

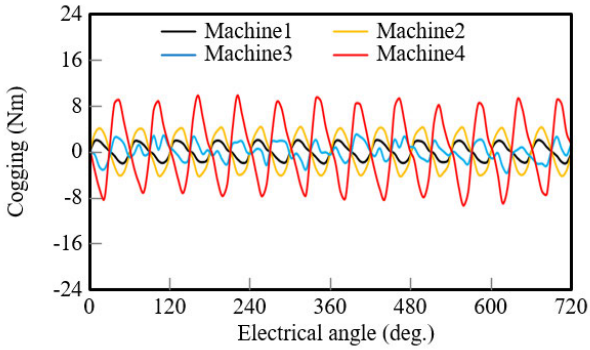


**FIGURE 15.** Cogging torque.

**TABLE 3.** Performance comparision.

| Items | Unit | Machine 1 | Machine 2 | Machine 3 | Machine 4 |
|---|---|---|---|---|---|
| Torque | Nm | 32.7 | 45 | 54.61 | 62.1 |
| Cogging (peak to peak) | Nm | 4.04 | 8.56 | 6.5 | 19.17 |
| Torque ripple | % | 6.3 | 7 | 3.6 | 10.1 |
| No-load back emf | V | 412.4 | 503 | 484.6 | 550 |
| Copper loss | W | 69.6 | 69.6 | 69.6 | 69.6 |
| Core loss | W | 238.86 | 240.84 | 201.8 | 235.76 |
| Efficiency | % | 89.9 | 92.4 | 94.4 | 94.5 |
| PM volume | $mm^3$ | 85860 | 111780 | 176805 | 176805 |
| PM Utilization | $Nm/mm^3$ | $3.81*10^{-4}$ | $4.03*10^{-4}$ | $3.09*10^{-4}$ | $3.51*10^{-4}$ |
| Cost of copper | HKD | 145 | 145 | 145 | 145 |
| Cost of PMs | HKD | 297.35 | 387.12 | 612.3 | 612.3 |
| Cost of iron core | HKD | 129.65 | 129.65 | 129.61 | 129.61 |
| Total cost | HKD | 572 | 661.77 | 886.91 | 886.91 |
| Torque density | $Nm/mm^3$ | $1.91*10^{-5}$ | $2.63*10^{-5}$ | $3.19*10^{-5}$ | $3.63*10^{-5}$ |

As shown in Table 3, Machine 4 has the highest efficiency and torque density. Machine 1 has the smallest PM volume and lowest cost. Compared to Machine 1, the torque density of Machine 4 also increases a lot. It is increased about 94.51%. And the torque density of Machine 3 also increases 60.37% when it compares to Machine 1. The total cost of each machine is also summarized in Table 3. It is clear that, Machine 3 and Machine 4 have the highest cost,

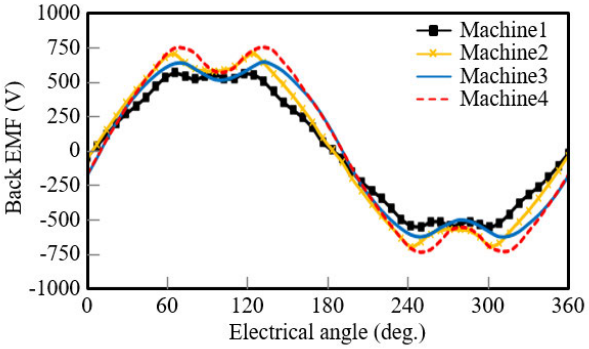


**FIGURE 16.** No-load back emf.

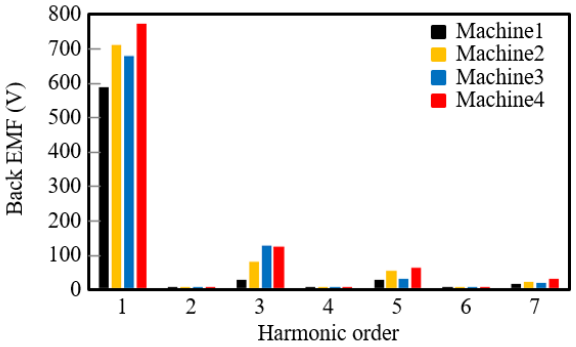


**FIGURE 17.** FFT results of no-load back emf.

which is mainly caused by the increased cost of PMs from 297.35 HKD to 612.3 HKD. Compared to Machine 1, the total cost of Machine 2 is increased 15.7% while Machine 3 and Machine 4 are increased 55%.

Fig. 16 compares the no-load back emf among all structures. It can be seen that, due to the harmonic effect, the distortion of the waveform is a little bit obvious. It is clear that, with the amplitude of the no-load back emf increases, the distortion also increases. According to Fig. 17, Machine 4 has the highest amplitude and relative high harmonic which is 17.77% while Machine 1 has the lowest amplitude and minimum harmonic which the THD is around 6.26%.

## V. ANALYSIS OF DESIGN PARAMETERS

Compared with other structures, Machine 4 has the highest torque density and efficiency. However, the torque ripple and the distortion of no-load back emf are quite high. To further investigate the possibility of torque performance improvement in Machine 4, the analysis of design parameters is carried out. The key design parameters such as outer diameter, inner diameter of the rotor and the air gap length are kept the constant. The related design parameters for the analysis are specified in Fig. 18. Considering the mechanical constrains and the rationality of the design, the ranges of the parameters are listed in Table 4.

The rotor PM pole arc coefficient is given by

$$\alpha_1 = \frac{W_{pm1} + W_{pm2} * 2}{W_{rt} + W_{pm1} + 2 * W_{pm2}} \tag{16}$$

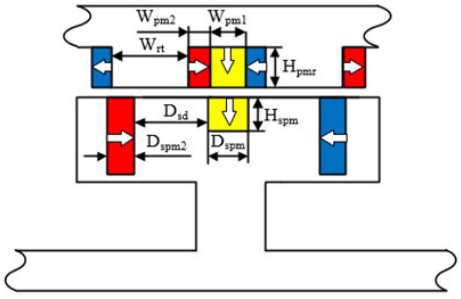


**FIGURE 18.** Description of geometric parameters.

**TABLE 4.** Range of parameters.

| Design Parameter | Unit | Value |
|---|---|---|
| $H_{pmr}$ | mm | 2.5-7.5 |
| $\alpha_1$ | / | 0.35-0.75 |
| $\alpha_2$ | / | 0.15-0.33 |
| $D_{spm}$ | deg | 4-12 |
| $H_{spm}$ | mm | 4-12 |
| $D_{sd}$ | deg | 14-19 |
| $D_{spm2}$ | deg | 4-8 |

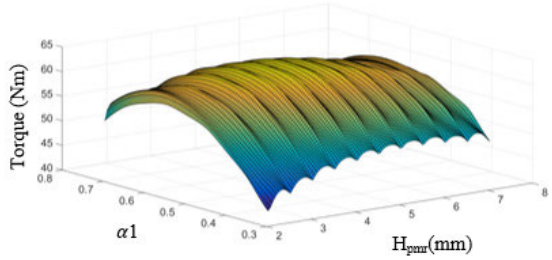


(a)

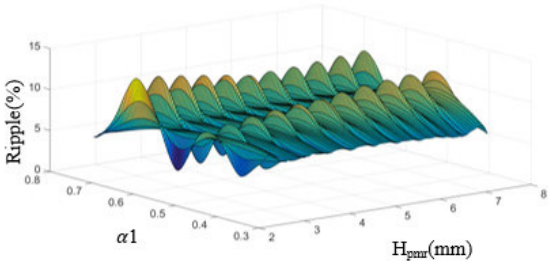


(b)

**FIGURE 19.** Torque performance under different $H_{pmr}$ and $\alpha_1$. (a) Output torque. (b) Torque ripple.

The Halbach coefficient is given by

$$\alpha_2 = \frac{W_{pm2}}{W_{pm1} + 2 * W_{pm2}} \tag{17}$$

The $H_{pmr}$ and $\alpha_1$ are changed at the same time. According to Fig. 19(a), the output torque increases with $H_{pmr}$ of the rotor PM until $H_{pmr}$ is equal to 4.5mm. The trend of torque regarding changes with $\alpha_1$ is the same as the height of rotor PM. The output torque increases first then decreases. Fig. 19(b) shows the ripple of different $H_{pmr}$ and $\alpha_1$, it is clear that the $\alpha_1$ is critical for the torque ripple.

Fig. 20 shows the torque performance under different $H_{pmr}$ and $\alpha_2$. It is obvious that with $H_{pmr}$ increases, the output

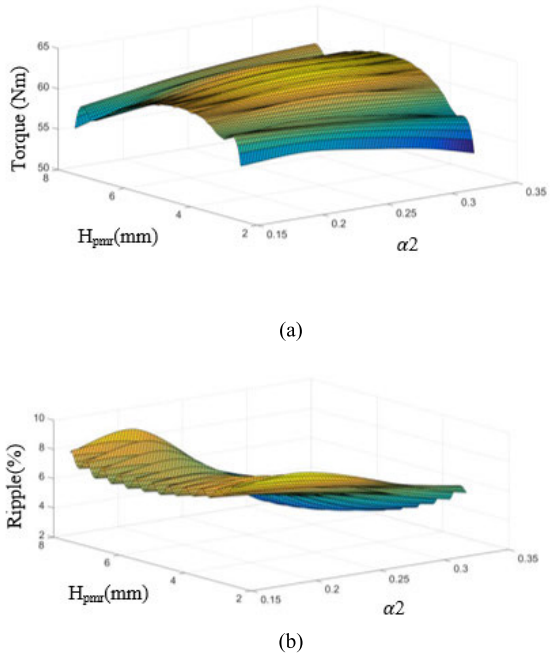


**FIGURE 20.** Torque performance under different $H_{pmr}$ and $\alpha_2$. (a) Output torque. (b) Torque ripple.

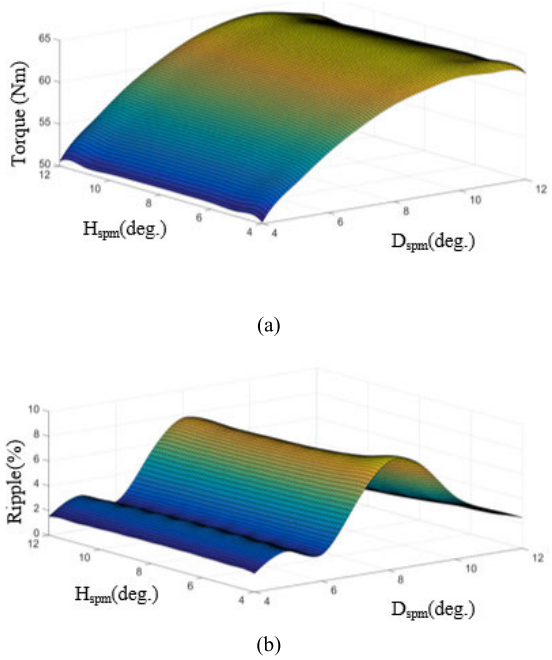


**FIGURE 21.** Torque performance under different $H_{spm}$ and $D_{spm}$. (a) Output torque. (b) Torque ripple.

torque increases then slightly decreases. The trend of $\alpha_2$ is totally the same but the change is not very obvious.

Fig. 21 shows the influence of different $D_{spm}$ and $H_{spm}$ combination to the torque performance. We can observe that if we keep the $D_{spm}$ in a constant value and increase $H_{spm}$, the output torque and ripple keep in a stable level and do not change too much. However, the torque will be increased with $D_{spm}$ is increased when $H_{spm}$ keeps the constant value. And the torque ripple will be increased and then decreased with $D_{spm}$ increased while $H_{spm}$ keeps constant.

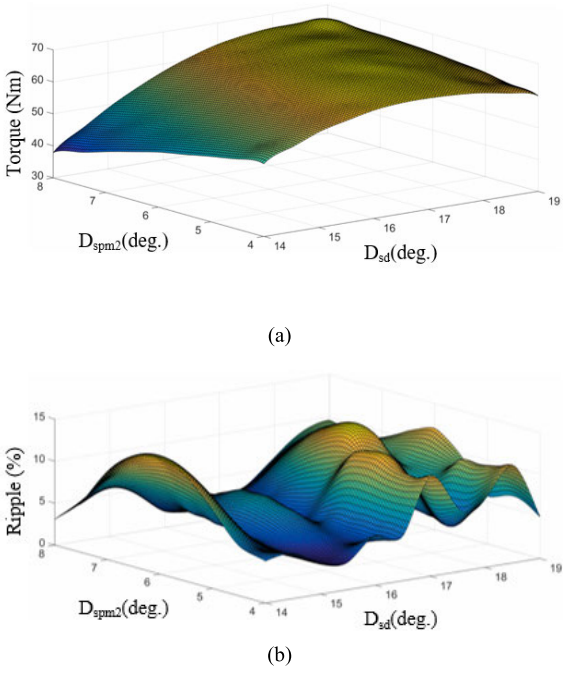


**FIGURE 22.** Torque performance under different $D_{sd}$ and $D_{spm2}$ (a) Output torque. (b) Torque ripple.

**TABLE 5.** Design parameters and performance of initial and final model.

| Parameter | Initial value | Final value |
|---|---|---|
| Machine outer diameter (mm) | 220 | |
| Rotor inner diameter (mm) | 90 | |
| Rotor PM thickness (mm) | 5 | 4.5 |
| Rotor PM pole arc coefficient | 0.5 | 0.6 |
| Halbach coefficient | 0.2 | 0.25 |
| Stator mid PM height (mm) | 8 | 8 |
| Stator mid PM width (deg) | 8 | 10 |
| Stator side PM width (deg) | 6 | 6 |
| Stator teeth width $D_{sd}$ (deg) | 16.5 | 16.5 |
| Torque (Nm) | 62.1 | 65.5 |
| Torque ripple (%) | 10.1 | 3.3 |
| Torque density (Nm/mm$^3$) | $3.63*10^{-5}$ | $3.83*10^{-5}$ |
| Efficiency (%) | 94.5 | 94.7 |
| PM volume (mm$^3$) | 176805 | 188536.6 |
| Cost of PMs (HKD) | 612.3 | 652.94 |
| Cost of iron core (HKD) | 129.61 | 128.65 |
| Total cost (HKD) | 886.91 | 926.15 |

The relationship between the torque performance and combinations of $D_{spm2}$ and $D_{sd}$ is shown in Fig. 22. It is clear that, the torque increases first then decreases when we keep $D_{spm2}$ constant. It can also be found that with the difference in $D_{spm2}$, the turning points of the total trend are different, the thicker of $D_{spm2}$, the higher value of turning points. This is due to the saturation effect in the modulation teeth between the stator mid PM and side PM. It can also be observed that, when $D_{sd}$ . is stable, the overall trend of the ripple is increased first and then decreased, with the increases of $D_{spm2}$.

Considering the usage of PMs volume, output torque and torque ripple, the final model can be obtained. The initial and final design parameters and performance are listed in Table 5. And Fig. 23 compares the output torque waveforms with the initial and final design parameters.

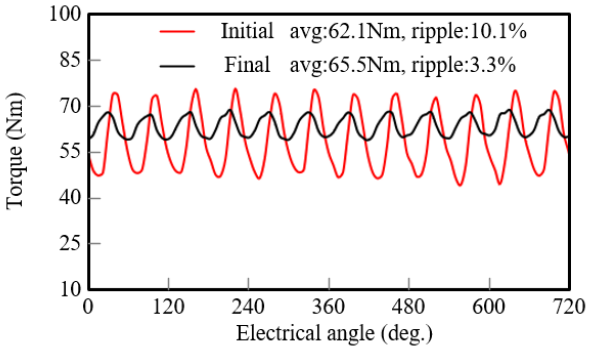


**FIGURE 23.** Torque comparison between initial and final model.

It can be seen that the final model has higher average output torque and lower torque ripple. The output torque increases about 5.6% while the torque ripple reduces 67.3% from 10.1% to 3.3%. With the torque density increasing, the efficiency also has a slight rise, from 94.5% to 94.7%.

## VI. CONCLUSION

This paper has presented and compared several PM arrangements in flux modulated machines. The working principle of the proposed machines with different PM arrangement is clearly illustrated through analyzing the working harmonics of each excitation source. FEM software is adopted to analyze the machine performance and verify the analytical calculation. The result shows when we adopt all three groups of PMs together, the flux modulated machine has the highest torque density and efficiency. The output torque of Machine 4 increases 100.3% compared with Machine 1 which only adopts one group PM. However, the parametrical analysis of the main dimensions is limited, the global optimization of this machine can be conducted in the future work.

## REFERENCES

[1] X. Liu, H. Chen, J. Zhao, and A. Belahcen, "Research on the performances and parameters of interior PMSM used for electric vehicles," *IEEE Trans. Ind. Electron.*, vol. 63, no. 6, pp. 3533–3545, Jun. 2016.
[2] G. Pellegrino, A. Vagati, P. Guglielmi, and B. Boazzo, "Performance comparison between surface-mounted and interior PM motor drives for electric vehicle application," *IEEE Trans. Ind. Electron.*, vol. 59, no. 2, pp. 803–811, Feb. 2012.
[3] K. T. Chau, C. C. Chan, and C. Liu, "Overview of permanent-magnet brushless drives for electric and hybrid electric vehicles," *IEEE Trans. Ind. Electron.*, vol. 55, no. 6, pp. 2246–2257, Jun. 2008.
[4] X. Zhao, S. Niu, and W. Fu, "Sensitivity analysis and design optimization of a new hybrid-excited dual-PM generator with relieving-DC-saturation structure for stand-alone wind power generation," *IEEE Trans. Magn.*, vol. 56, no. 1, pp. 1–5, Jan. 2020.
[5] Y. Fan, J. Huang, X. Han, X. Fu, and H. Wei, "Design, analysis and sensorless control of a new self-decelerating permanent-magnet motor," in *Proc. IECON 38th Annu. Conf. IEEE Ind. Electron. Soc.*, Oct. 2012, pp. 4104–4109.
[6] Y. Fan, L. Zhang, M. Cheng, and K. T. Chau, "Sensorless SVPWM-FADTC of a new flux-modulated permanent-magnet wheel motor based on a wide-speed sliding mode observer," *IEEE Trans. Ind. Electron.*, vol. 62, no. 5, pp. 3143–3151, May 2015.
[7] A. Toba and T. A. Lipo, "Novel dual-excitation permanent magnet Vernier machine," in *Proc. Conf. Rec. IEEE Ind. Appl. Conf. 34th IAS Annu. Meeting*, Oct. 1999, pp. 2539–2544.
[8] X. Zhao, S. Niu, and W. Fu, "Torque component quantification and design guideline for dual permanent magnet Vernier machine," *IEEE Trans. Magn.*, vol. 55, no. 6, pp. 1–5, Jun. 2019.
[9] D. Li, R. Qu, and T. A. Lipo, "High-power-factor Vernier permanent-magnet machines," *IEEE Trans. Ind. Appl.*, vol. 50, no. 6, pp. 3664–3674, Nov. 2014.
[10] B. Kim and T. A. Lipo, "Analysis of a PM Vernier motor with spoke structure," *IEEE Trans. Ind. Appl.*, vol. 52, no. 1, pp. 217–225, Jan. 2016.
[11] C.-C. Hwang, C.-M. Chang, S.-S. Hung, and C.-T. Liu, "Design of high performance flux switching PM machines with concentrated windings," *IEEE Trans. Magn.*, vol. 50, no. 1, pp. 1–4, Jan. 2014.
[12] Z. Q. Zhu, J. T. Chen, Y. Pang, D. Howe, S. Iwasaki, and R. Deodhar, "Analysis of a novel multi-tooth flux-switching PM brushless AC machine for high torque direct-drive applications," *IEEE Trans. Magn.*, vol. 44, no. 11, pp. 4313–4316, Nov. 2008.
[13] C. Yu, S. Niu, S. L. Ho, and W. N. Fu, "Design and analysis of a magnetless double-rotor flux switching motor for low cost application," *IEEE Trans. Magn.*, vol. 50, no. 11, pp. 1–4, Nov. 2014.
[14] Y. Liao, L. Xu, and L. Zhen, "Design of a doubly fed reluctance motor for adjustable-speed drives," *IEEE Trans. Ind. Appl.*, vol. 32, no. 5, pp. 1195–1203, 1996.
[15] D. G. Dorrell, A. M. Knight, and R. E. Betz, "Improvements in brushless doubly fed reluctance generators using high-flux-density steels and selection of the correct pole numbers," *IEEE Trans. Magn.*, vol. 47, no. 10, pp. 4092–4095, Oct. 2011.
[16] Y. Wang, S. L. Ho, W. N. Fu, and J. X. Shen, "A novel brushless doubly fed generator for wind power generation," *IEEE Trans. Magn.*, vol. 48, no. 11, pp. 4172–4175, Nov. 2012.
[17] K. Atallah and D. Howe, "A novel high-performance magnetic gear," *IEEE Trans. Magn.*, vol. 37, no. 4, pp. 2844–2846, Jul. 2001.
[18] Y. Chen, W. Fu, and X. Weng, "A concept of general flux-modulated electric machines based on a unified theory and its application to developing a novel doubly-fed dual-stator motor," *IEEE Trans. Ind. Electron.*, vol. 64, no. 12, pp. 9914–9923, Dec. 2017.
[19] R. Hosoya and S. Shimomura, "Apply to in-wheel machine of permanent magnet Vernier machine using NdFeB bonded magnet—Fundamental study," in *Proc. 8th Int. Conf. Power Electron. ECCE Asia*, May 2011, pp. 2208–2215.
[20] Y. Tasaki, R. Hosoya, Y. Kashitani, and S. Shimomura, "Design of the Vernier machine with permanent magnets on both stator and rotor side," in *Proc. 7th Int. Power Electron. Motion Control Conf.*, Jun. 2012, pp. 302–309.
[21] Q. Lin, S. Niu, and W. N. Fu, "Design and optimization of a dual-permanent-magnet Vernier machine with a novel optimization model," *IEEE Trans. Magn.*, vol. 56, no. 3, pp. 1–5, Mar. 2020.
[22] Q. Wang, S. Niu, and L. Yang, "Design optimization and comparative study of novel dual-PM excited machines," *IEEE Trans. Ind. Electron.*, vol. 64, no. 12, pp. 9924–9933, Dec. 2017.
[23] T. Fukami, Y. Ueno, and K. Shima, "Magnet arrangement in novel flux-modulating synchronous machines with permanent magnet excitation," *IEEE Trans. Magn.*, vol. 51, no. 11, pp. 1–4, Nov. 2015.
[24] J. Li, K. Wang, and H. Zhang, "Comparative analysis of spoke-type, consequent-pole and hybrid-pole permanent magnet machines," *IET Electr. Power Appl.*, vol. 14, no. 4, pp. 648–657, Apr. 2020.
[25] G. Zhao and W. Hua, "Comparative study between a novel multi-tooth and a V-shaped flux-switching permanent magnet machines," *IEEE Trans. Magn.*, vol. 55, no. 7, pp. 1–8, Jul. 2019.
[26] S. Wang, S. Niu, and W. Fu, "Comparative study of relieving-DC-saturation hybrid excited Vernier machine with different rotor pole designs for wind power generation," *IEEE Access*, vol. 8, pp. 198900–198911, 2020.
[27] X. Zhao and S. Niu, "Design and optimization of a new magnetic-geared pole-changing hybrid excitation machine," *IEEE Trans. Ind. Electron.*, vol. 64, no. 12, pp. 9943–9952, Dec. 2017.

**JIAHUI HUANG** received the B.Sc. degree in electrical engineering and automation from the Xiamen University of Technology, China, in 2013, and the M.Sc. degree in electrical engineering from The Hong Kong Polytechnic University, Hong Kong, in 2015, where she is currently pursuing the Ph.D. degree in electrical engineering.

Her main research interests include design, analysis, and optimization of electric machines.

**WEINONG FU** received the B.Eng. degree from the Hefei University of Technology, Hefei, China, in 1982, the M.Eng. degree from the Shanghai University of Technology, Shanghai, China, in 1989, and the Ph.D. degree from The Hong Kong Polytechnic University, Hong Kong, in 1999, all in electrical engineering. In 2007, he was one of the key developers with Ansoft Corporation, Pittsburgh, PA, USA. He has about seven years of working experience with Ansoft, focusing on the development of the commercial software Maxwell. He is currently a Professor with The Hong Kong Polytechnic University. He has authored or coauthored more than 240 articles in refereed journals. His current research interests mainly include numerical methods of electromagnetic field computation, optimal design of electric devices based on numerical models, applied electromagnetics, and novel electric machines.

**SHUANGXIA NIU** (Senior Member, IEEE) received the B.Sc. and M.Sc. degrees in electrical engineering from the School of Electrical Engineering and Automation, Tianjin University, Tianjin, China, and the Ph.D. degree in electrical engineering from the Department of Electrical and Electronic Engineering, The University of Hong Kong, Hong Kong. Since 2009, she has been with The Hong Kong Polytechnic University, Hong Kong, where she is currently an Associate Professor with the Department of Electrical Engineering. She has authored or coauthored more than 100 articles in leading journals. Her research interests include novel electrical machines and drives, renewable energy conversion systems, and applied electromagnetics.

**XING ZHAO** (Member, IEEE) received the B.Eng. degree in electrical engineering from the Nanjing University of Aeronautics and Astronautics, China, in 2014, and the Ph.D. degree in electrical engineering from The Hong Kong Polytechnic University, Hong Kong SAR, in 2020. From July 2019 to January 2020, he was a Research Scholar with the Center for Advanced Power Systems, Florida State University, USA. Since July 2020, he has been with the Department of Electrical Engineering, The Hong Kong Polytechnic University, where he currently holds a position of Research Assistant Professor. He has published more than 25 technical articles in leading journals and holds six granted patents. His research interests include electrical machines, motor drives, and power electronics for electric propulsion and renewable energy systems. He is an Associate Editor of IEEE OPEN JOURNAL OF INDUSTRIAL ELECTRONICS SOCIETY.